Applied Surface Science 510 (2020) 145216

Contents lists available at ScienceDirect

Applied Surface Science

journal homepage: www.elsevier.com/locate/apsusc

Full Length Article

Experimental and theoretical interpretation of the order/disorder clusters in CeO_2:La

Leandro Silva Rosa Rocha[a,*], Rafael Aparecido Ciola Amoresi[b], Thiago Marinho Duarte[c,d], Naiara Letícia Marana[d], Julio Ricardo Sambrano[d], Celso Manuel Aldao[e], Alexandre Zirpoli Simões[b], Miguel Adolfo Ponce[e], Elson Longo[a]

[a] Federal University of Sao Carlos (UFSCar), Department of Chemistry, São Carlos, SP, Brazil
[b] Sao Paulo State University (UNESP), School of Engineering, Guaratinguetá, SP, Brazil
[c] LACOM/INCTMN, Federal University of Paraiba, João Pessoa, PB, Brazil
[d] Sao Paulo State University (UNESP), School of Sciences, Bauru, SP, Brazil
[e] Institute of Materials Science and Technology (INTEMA), Mar del Plata, Argentina

ARTICLE INFO

Keywords:
Defects
Lanthanum
Cerium oxide
Carbon monoxide
X-ray photoelectron spectroscopy

ABSTRACT

A spectroscopic study of nanostructured lanthanum-doped cerium oxide samples showed that a mild decrease by 5.3% in the surface concentration of Ce(III) species and, a reduction by 0.2 eV in the so-called energy-gap (E_F – E_v) after lanthanum addition was sufficient to create the previously reported significant dual behavior when exposed to carbon monoxide at 653 K. The observed X-ray diffraction patterns indicated the presence of a pure fluorite-type crystalline structure. A higher presence of paramagnetic defects clusters, indicated by electron paramagnetic resonance spectroscopy measurements and confirmed by the X-ray photoelectron spectroscopy, was attributed as being responsible for its dual behavior in a $CO_{(g)}$ atmosphere. Theoretical studies have shown the band structure and density of state of the pure and doped material, illustrating the orbitals that participate in the valence band and conduction band. The addition of a small quantity of La^{3+} converted some Ce^{3+} into Ce^{4+}, narrowed the "effective band-gap" by 0.2 eV, and created a singly ionized oxygen vacancy species, thus changing the total electrical resistance and creating its dual behavior. The exposure to a reducing atmosphere such as carbon monoxide resulted in a significant increase in defects and converted some Ce^{4+} into Ce^{3+} and vice-versa with oxygen atmosphere exposure.

1. Introduction

Ceria(CeO_2)-based nanomaterials consist of one of the most reactive rare-earth oxides that, when modified with cations of distinct valence, present an n-type semiconductor behavior with a band-gap around 6 eV. However, owing to its unique physicochemical properties [1], attributed to the electronic configuration of cerium atoms ([Xe] $4f^15d^16s^2$), this material has been extensively considered for applications, including catalysis [2], fuel cells [3], photocatalysis [4], hydrogen storage [5] and polishing materials [6], and chemical sensors [7].

Distinct approaches have been employed to prepare CeO_2-based compounds for environmental sensing applications. Recent reports have investigated the utilization of hybrid heterostructures such as reduced graphene oxide (RGO)-CeO_2 [8] and CeO_2-B_2O_3 (B = Fe, Cr) [9] for NO_2 monitoring, hybrid CeO_2-perovskite type sensing electrodes for acetone [10], and polyaniline (PANI)-CeO_2 nanocomposites for ammonia detection [11]. However, virtually no attention has been given to the detection and monitoring of carbon monoxide (CO), which has been termed "the unnoticed poison of the 21st century" [12] owing to several cases of unintentional intoxication worldwide [13]. The approximately 102.000 cases of emergency department visits for CO intoxication during 2003–2013, in the USA [14], emphasize the need for prevention efforts such as the use of CO alarms and adequate use and maintenance of fuel and gas-powered devices.

Regarding the mechanisms behind the detection of gases using nanostructured materials, the interactions generated on a semiconductor surface when exposed to certain atmospheres must be considered. In a reducing atmosphere such as CO with temperatures above 473 K, oxygen species can be withdrawn from a bulk and diffuse towards the surface [15]. Consequently, oxygen vacancies are created along with a reduction of Ce(IV) to Ce(III) [16]. In fact, upon formation of a single

* Corresponding author.
E-mail address: leandro.rocha@liec.ufscar.br (L.S.R. Rocha).

https://doi.org/10.1016/j.apsusc.2019.145216
Received 17 September 2019; Received in revised form 4 November 2019; Accepted 27 December 2019
Available online 13 January 2020
0169-4332/

Ce(III) ion, there must be an energy reduction because of the relaxation of the neighboring O^{2-} ions, and this tiny polarization is sufficient enough to trap charge carriers in localized configurations constituting polarons that are responsible for the conduction phenomenon [17]. Therefore, the ability to release or uptake oxygen species dictates the applicability of ceria-based materials for environmental and energy-related applications and depends on the Ce(IV)/Ce(III) ratio, which in turn depends on the concentration and types of oxygen vacancies and other defects within the lattice structure [18]. In addition, a size variation in lattice parameters exists because of the difference in the Ce(III) and Ce(IV) ionic radii (128 and 111 pm, respectively) that results in the development of strains that directly influence their properties [19]. Once a gas interacts with a film surface, interfacial characterizations are critical for understanding the underlying conduction mechanisms.

Regarding electrical conduction, it has been widely accepted that, in numerous polycrystalline semiconductor materials, potential barriers of a Schottky-type nature are formed at particle or grain interfaces. These barriers govern the electrical properties and any adsorbed or interacting species at the surface can induce changes in the barrier heights as well as in the concentration of its carriers [20]. Most researchers consider that many semiconductor oxides have a large number of oxygen vacancies [21], that determine their n-type character. However, rare-earth oxides with 4f-shells of lanthanide ions are likely to present narrow electronic bands, and therefore, their electrical conduction involve 4f electrons that migrate by an activated hopping mechanism of polarons [22]. This was indicated by shreds of evidence such as low electron mobility (μ) and an independence of the Seebeck coefficient with temperature, which contrasts with a band model that predicts a term as (−1/T) [23].

Our group developed a La-doped CeO_2 compound [24], obtained by the microwave-assisted hydrothermal (MAH) technique that presented a significant dual response when exposed to CO and had a quick electric response-time (t_{resp}) of approximately 5 s and an extremely fast optical reply of approximately 0.3 s that reversibly changed its surface color at a temperature close to 673 K. This work aims to expand the knowledge regarding how structural defects such as oxygen vacancies and reduced Ce(III) species affect the electronic properties of La-doped CeO_2 films and to generate their visible phenomena when exposed to a CO atmosphere.

2. Experimental procedures

2.1. Nanopowders preparation and characterization

Pure and La-doped ceria nanopowders were obtained by a MAH technique, starting with the dissolution of 0.15 M Cerium (III) nitrate hexahydrate ($Ce(NO_3)_3{\cdot}6H_2O$, 99%, Sigma-Aldrich) in distilled water under magnetic stirring. In another beaker, lanthanum oxide (La_2O_3) (99%, Sigma-Aldrich) was dissolved under constant stirring and heating (343 K) assisted by nitric acid (HNO_3, 65%, Labsynth) and added to the former solution. The resulting mixture with a pH of 10 was adjusted with potassium hydroxide (2 mol L^{-1}, 99.5%, Labsynth). The solution was poured into a sealed Teflon autoclave, placed in a microwave reaction vessel (Panasonic NN-ST357WRP, 2.45 GHz, 800 W), heat-treated at 373 K for 8 min (10 K/min), and then naturally cooled. The solutions were centrifuged three times (10 min, 2.000 rpm) to separate the precipitated oxide from the supernatant, washed with deionized water, and dried at 373 K for 48 h in a laboratory oven (Solidsteel, SSA85L).

The pure and La-doped ceria (CeO_2) powders obtained are referred to as P.C and L.D.C, respectively, for ease of use. They were structurally characterized by X-ray diffraction (XRD) with data collected by a Rigaku-Dmax/2500PC with a Cu-Kα radiation λ = 1.5406 Å in the 2θ range of 20–80° in room temperature. The mean crystallite size (d) was calculated using the Scherrer method as (Kxλ)/(βxcosθ), where K is the shape-factor (we used 0.94 because it is a good approximation for cubic symmetries), λ is the X-ray wavelength, β is the full width at half maximum (FWHM) in radians obtained with the aid of open-source software QtiPlot (0.9.8.9 svn 2288, 02/11/2011) by a Lorentzian fit of the (1 1 1) peaks, and θ is the diffraction angle of the main peak [25]. The Williamson-Hall method was used to measure the microdeformation [26,27]. To ensure the prepared samples' purity, a commercial cerium(IV) oxide with 99.9% purity from Sigma-Aldrich, named "S.A", was used as a comparison. The electron paramagnetic resonance (EPR) spectra of the P.C and L.D.C samples were recorded on a Bruker EMX-300 spectrometer operating at X-band (9 GHz) with a microwave power of 2 mW, an amplitude modulation of 1Gauss, time constant of 2.56 ms, conversion time of 10.24 ms, and modulation frequency of 100 kHz. The g-factor was referenced with respect to $MgO:Cr^{3+}$ (g = 1.9797) as the external standard. An EPR measurement was performed at room temperature (298 K), and the spectra were evaluated using the SimFonia program.

Ultraviolet–visible (UV–Vis) spectra were collected by a Varian (Cary 5G) at the Sao Paulo State University (UNESP), Institute of Chemistry, Araraquara, Brazil, in the diffuse reflectance mode with a wavelength in the range of 200–800 nm. The effective band gap (E_g) energy was obtained by means of a Tauc's plot that provided an estimation of E_g as shown in Eq. (1):

$$(h\nu\alpha)^{1/n} = A(h\nu - E_g) \quad (1)$$

where α is the absorption coefficient, $h\nu$ is the photon energy, A is the band-tail parameter, and E_g is the band gap energy. The nature of the electronic transitions provided the following values: direct allowed (n = 1/2), direct forbidden (n = 3/2), indirect allowed (n = 2) and indirect forbidden (n = 3). Therefore, considering a direct allowed transition, we have Eq. (2):

$$(h\nu\alpha)^2 = A(h\nu - E_g) \quad (2)$$

To complement our understanding of both P.C and L.D.C systems in terms of their electronic-band structures and respective density of states (DOS), DFT simulations were conducted using the CRYSTAL17 program [28] with the WC1LYP (8% hybrid) functional. The oxygen atoms were described by all-electron basis set O_6-31d1 [29], cerium atoms were described by means of the effective core pseudopotential (ECP) basis set, the Ce_ECP basis set [30]. To simulate the CeO_2:La doped, a 2 × 2 × 2 supercell (using a conventional cell) of 32 and 64 Ce and O atoms, respectively, was generated and two Ce atoms were symmetrically substituted by two La atoms in the crystal lattice. The band structures were obtained for 100 K points along the appropriate height-symmetry paths of the adequate Brillouin zone, and the DOS diagrams were calculated to analyze the corresponding electronic structure. To analyze the changes on structural and electrical properties, the CeO_2:La model was compared with the undoped CeO_2 supercell.

2.2. Sensor film preparation and characterization

Thick films were manually deposited using the obtained P.C and L.D.C powders through a low-cost *screen-printing* technique using glycerin (Glycerol p.a., ACS reagent, Labsynth) in a solid/ligand ratio of 30 mg/0.05 mL. The substrates were prepared as described in a previous work [31]. The sensor film thicknesses were 58 and 56 μm for the P.C and L.D.C samples, respectively. As previously mentioned, the alumina substrates were electrically measured and exhibited an insulating behavior with no influence on the film electrical response [32]. The complex impedance spectroscopy (CIS) of the films was monitored using an HP4284A impedance analyzer in a closed device for the optoelectronic characterization of materials, under patent in Brazil (BR102016028383) and Argentina (AR103692). The measurement was made at 673 K, chosen because of the color change phenomenon, that occurred in the L.D.C sample [24]. Atmospheric changes were performed from vacuum to 50 mmHg of synthetic air (20% O_2) and CO

atmospheres. For measurements during atmospheric exposure, a 1-mA magnitude of excitation current was applied by the two-point probe technique with an AC-type measurement in a frequency interval of 20 Hz–1 MHz.

Because of the applied current range, the electrode capacitance contribution can be ignored [24]. To ensure that the electric response was exclusively generated by the exposure to the different atmospheres, the films were thermally treated three times in a dry-air-closed-atmosphere up to 653 K with a 1 K/min rate and maintained for 2 h. Therefore, no traces of humidity or glycerol (boiling point at 760 mmHg: 563 K [33]) influenced the measurements.

X-ray photoemission spectroscopy (XPS) measurements were performed for the surface characterization with a *Scienta Omicron ESCA* + spectrometer system equipped with a hemispherical analyzer EA125 and an Al Kα (hn = 1486.7 eV) monochromatic source. The source used 280 W, while the spectrometer worked at a constant pass energy mode of 50 eV. All data analysis was performed using CASA XPS Software (Casa Software Ltd, UK) with the spectra pretreated by performing a Shirley background subtraction [34] with the baseline encompassing the entire spectrum and correcting the charge effects using the C 1 s peak at 285.0 eV as the charge reference. The peak fitting was performed using a Semi-Voigt function (convoluted Gaussian-Lorentzian line shapes) with a constant ratio between spin-orbit splitting components to determine the area of each peak corresponding to the signals from Ce^{3+} and Ce^{4+}. The peaks were fitted in a series of iterations that allowed the areas and their FWHMs to vary throughout all steps with their locations varying up to 0.1 eV, because of the nanoscale nature of the materials during the last iteration [35,36].

3. Results and discussion

3.1. X-rays diffraction analysis

Fig. 1 shows a comparison of the XRD analysis of the $Ce_{1-(3/4)x}La_xO_2$ powders (x = 0.00 and 0.08) obtained by the MAH technique at 373 K for 8 min and the spectra of the commercial Sigma-Aldrich (S.A) sample.

All three spectra clearly show the characteristic peaks of the CeO_2 fluorite-like cubic structure (JCPDS 34-0394) with a space group *Fm*-3*m*, theoretical lattice constant $a = b = c = 5.411$ Å and no trace of impurities or secondary phases indicating an isomorphic substitution of cerium (Ce^{4+}) atoms by lanthanum (La^{3+}) along with a complete conversion of the precursors into the desired oxides. We propose the modified Eqs. (3)–(5) to clarify the complete conversion of the precursors hydrolisys into the final products as reported by Hirano and Inagaki [37]. We precipitated the white-colored hydrated hydroxides (visible to the naked eye during the experiment) when pH-adjusted with potassium hydroxide, then used microwave radiation to deprotonize and convert them into oxides.

$$Ce(NO_3)_3{\cdot}6H_2O \rightarrow Ce^{3+} + 3NO_3^- + 6H_2O \quad (3)$$

Table 1
Mean crystallite size (D), lattice constant (*a*), and lattice strain of nanopowders, calculated by Scherrer, Bragg and Williamson-Hall methods.

Sample	$2\theta_{(1\ 1\ 1)}$ (°)	FWHM (°)	a (Å)	D (nm)	Lattice strain
S.A	28.46	0.847	5.43	10.11	0.0146
P.C	28.56	0.517	5.41	16.56	0.0089
L.D.C	28.36	0.821	5.62	10.42	0.0142

$$Ce^{3+} + x.OH + y \cdot H_2O \rightarrow [Ce(OH)_x(H_2O)_y]^{(3-x)+} \quad (4)$$

$$[Ce(OH)_x(H_2O)_y]^{(3-x)+} + H_2O \rightarrow CeO_2{\cdot}nH_2O + nH_2O + H_3O^+ \quad (5)$$

When comparing our samples to the pure CeO_2 obtained by K. Polychronopoulou et al. [38], in which some carbonate ($Ce(OH)_x(CO_3)_y$) peaks were observed, and to the 3 and 6% wt. Fe-doped cerium oxides in which secondary phases of $CeFeO_3$ were also present [39], the purity of our samples was bolstered. The P.C and L.D.C samples prepared by the MAH technique had higher intensities in the (1 1 1) planes than those of the Sigma-Aldrich (S.A) sample, strengthening the capability of the MAH technique to produce highly-ordered polycrystalline nanomaterials with short reaction times and temperatures. This feature can also be recognized from the lattice strain measurements that indicate a reduced long-range disorder (virtually no stacking faults at (1 1 1) direction) for the P.C sample when compared to the S.A and L.D.C samples. The mean crystallite size (D) calculated by the Scherrer equation, along with the lattice constant *a* (Å) and the induced lattice strain from crystal imperfections and distortions, given by the expression FWHM/(4.tan θ) [40], are shown in Table 1.

The La-doped CeO_2 had a reduced mean crystallite size compared to that of the pure sample, despite the La^{3+} ions having a higher ionic radius (0.110 nm) than that of Ce^{4+} (0.097 nm) [41]. This could be the result of the use of nitric acid (HNO_3) during the La_2O_3 dissolution, which during dissociation generates more nitrate ions $(NO_3)^-$ that interact with potassium ions (K^+) to form potassium nitrate (KNO_3), which in turn surrounds the nucleated La-doped CeO_2 particles and inhibits their growth [42].

3.2. Electron paramagnetic resonance spectroscopy

The room-temperature EPR spectra are shown in Fig. 2. In general, EPR signals of CeO_2 can result from oxygen species adsorbed onto Ce^{4+} ions or from filled oxygen vacancies to form surroundings with different symmetries [43]. Both spectra have similar behaviors typical of samples with unpaired electrons that correspond to only one absorption event plotted as its first derivative. The observed signal in a magnetic field close to $B_0 = 3.388$ G regarding the presence of paramagnetic species such as Ce^{3+} ([Xe] $4f^1$ $5d^0$) was in accordance with the reports of Ratnasamy et al. [44] and Araújo et al. [45]. Note that the electron configuration of Ce^{4+} with an atomic number (Z) = 54 corresponds to the [Xe] electron configuration, while the Ce^{3+} (Z = 55) electron

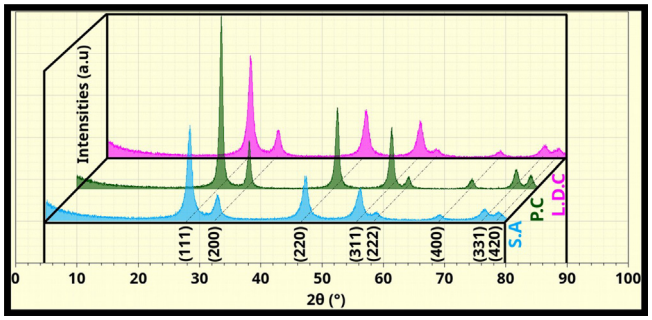

Fig. 1. XRD of the P.C and L.D.C samples obtained by the MAH technique compared to a commercial CeO_2 sample with 99.9% purity.

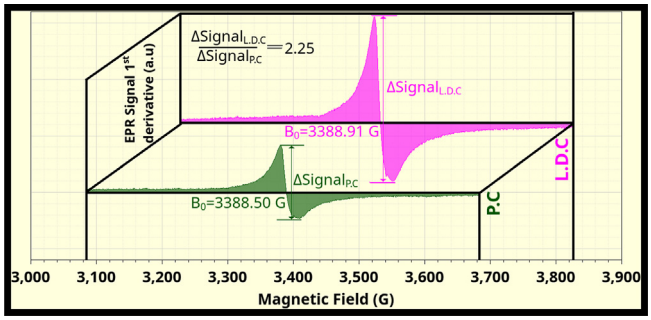

Fig. 2. EPR spectra of P.C and L.D.C samples obtained by MAH technique at 373 K for 8 min.

configuration is [Xe] $4f^1$. The La^{3+} electron configuration is similar to Ce^{+4} with no unpaired electrons, and therefore no paramagnetic signal is expected. The highly symmetrical peak pattern characteristic of an isotropic system is consistent with the high symmetry observed in the XRD results. The signal did not have the hyperfine structure coupling typical of materials with total spin (S) = ½ [46] with an augmented intrinsic amount of defects because of the substitution of cerium with lanthanum ions in a fluorite-type cubic structure. The signal can be ascribed to the transitions of $s = -1/2 \leftrightarrow s = +1/2$ from unpaired electrons of Ce^{3+} ions that are more energetically favorable owing to their structural defects [47] such as oxygen vacancies located in the nearest neighbor positions [48]. Once the first derivative spectra have identical line-shape widths, it is reasonable to consider a simple relation of the area = $(\text{width})^2 \times$ (height) as proportional to the content of the paramagnetic species [49,50]. In this way, the L.D.C sample had a signal ratio of 2.25 at B_0 in comparison to the P.C, likely indicating a higher amount of paramagnetic species. This is consistent with the assumption that a higher lanthanum concentration requires more oxygen vacancies likely described as complex clusters of the type $[CeO_7.V_O^{\cdot}]$ for charge compensation, which in turn distorts the local cubic symmetry. The EPR detection of complex defects in CeO_2 has been discussed in many publications [51–54] and relates mainly to a g-line of 2 observed from room to very high temperatures, which is not typical for rare-earth ions except for S-state ions. The g-factor was estimated from the relation $g_e = h.f/(B_0.\beta)$, where h corresponds to the Planck constant (6.62×10^{-34} J s), f the frequency of the radiation (9 GHz), β the Bohr magneton 9.274×10^{-24} J/T, and B_0 the magnetic field value at y = 0 (see Table 2).

The experimental g-factor (1.89) was slightly shifted from the theoretical g-value of 2 of the cubic site position of Ce^{3+} in the fluorite-type structure [55], indicating the existence of spin-orbit coupling [56]. The slightly shifted g-value can be ascribed to changes in the electron coupling of the surface superoxide-like species (O_2^-) because of the doping with La^{3+}, which further confirms that the La-doped sample possessed more singly ionized oxygen vacancies [57] and thus generate more surface-active oxygen species responsible for enhancing its gas sensing properties.

3.3. Ultraviolet–Visible spectroscopy, band structure and density of states

Fig. 3 shows the Tauc plots for the P.C and L.D.C samples along with their respective energy gaps. The plots with a tail-like shape suggest a non-uniform band gap structure with intermediary energy levels between the valence and the conduction bands. The L.D.C had a broader transition likely indicating more intermediate levels within the gap. The band-gap corresponds to the energy difference between the highest energy level of the valence band (E_v) and the lowest energy level of the conduction band (E_c). The energy bands of CeO_2 can be split into two: more densely filled oxygen 2p states below the Fermi level (E_F), and those above the E_F related to the cerium 5d states which define the band-gap magnitude [$\sim(E_c - E_v)$] as observed by density functional theory studies [58]. Recent studies, which best describe the electronic structure of ceria, have been performed and showed that the conduction band is mainly composed of Ce 4f states [59].

To completely address the electronic structure of these materials, we have performed theoretical simulations in order to verify the presence of 4f localized states. Fig. 4a and b show the band structure and DOS for the pure CeO_2, that were shifted on zero according to Fermi Energy.

Table 2
Experimental g-factors and their respective values of magnetic field B_0.

Sample	B_0 (T)	g-factor
P.C	3388.50×10^{-4}	1.8959
L.D.C	3388.91×10^{-4}	1.8957

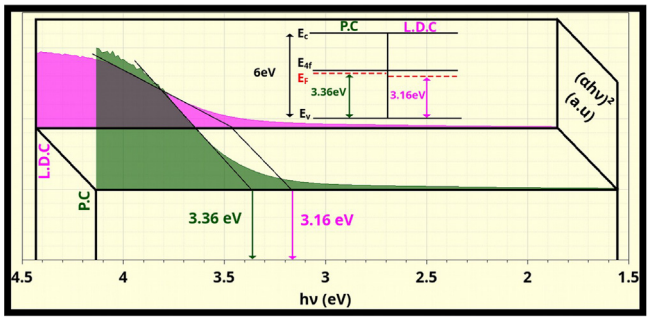

Fig. 3. UV–Vis spectra of the P.C and L.D.C samples obtained by MAH technique at 373 K for 8 min.

Fig. 5a shows a direct band gap at Γ point of 2.80 eV. The contribution to the DOS regarding O and Ce atoms is shown in Fig. 5b. As can be seen, the most contributor on the valence band maximum (VBM) is the 2p orbital of oxygen atoms, the three O-2p are degenerated and have no O-s contribution on this energy range. On VB, the Ce-p orbitals contribute less than O-2p, while the Ce-d presents contribution on the internal VB. In contrast, the most contributor on conduction band (CB) is the Ce-f orbitals, and Ce-$f_{(2z^2-3x^2-3y^2)z}$ orbital (Fig. 4c) presents the higher density of states. In this sense, the electron transition on undoped CeO_2 occurs between O-2p on VB and Ce-f on CB.

Fig. 5 show the band structures and the DOS of the La-doped CeO_2. A direct transition band gap at Γ point and a reduction of ~10% of the theoretical band gap energy were observed (Fig. 5a). According to the DOS analysis (Fig. 5b), after the La-doping, the O-2p stills the most contributor on VBM, although the contribution is less than the undoped-CeO_2. The reduction of O-2p contribution can be attributed to the La-sp contribution on VB, that is higher on VB than on CB. The influence of La-sp also reflects on Ce-d contribution, that was reduced on a half in this energy range, if compared with the undoped-CeO_2, and also on Ce-f displaced on CB. The Ce-f orbitals, with Ce-$f_{(2z^2-3x^2-3y^2)z}$ as the most contributor, were displaced in 0.12 eV, and the electron transition is between O-2p on VB and Ce-f on CB. Although a small separation observed between Ce-f orbitals (in ~2.80 eV) (Fig. 5c), previously degenerate on the undoped-CeO_2 ($f_{(x^2-3y^2)x}/f_{(3x^2-y^2)y}$, and $f_{(4z^2-x^2-y^2)x}/f_{(4z^2-x^2-y^2)y}$), the separation of these orbitals is not so significant as not to be considered (or proceed) degenerate after doping with La. Thus, these analyzes corroborate with the creation of localized energy-levels in the f-orbital of CB after doping with La [60–62].

Therefore, when working with ceria-based compounds in which electrons can be found in the $4f^1$ state, with an E_{4f} energy lower then E_{5d}, we might find an energy gap for electron transitions towards energy levels close to the 4f state, corresponding to the values around 3 eV above E_v [63]. Such a gap value can be related to the existence of intermediate transitions between O 2p and Ce empty 4f-states, as well as between Ce 4f states lying very close to the E_F and the Ce 5d states close to the conduction band (E_c). This is in accordance with theoretical simulations [64] as a consequence of the reduction from Ce(IV) to Ce(III) and the subsequent formation of oxygen vacancies [65,66]. Hence, the introduction of a trivalent cation (La^{3+}) in the lattice promotes a narrowing effect on the energy gap ($E_F - E_v$). As can be seen, experimentally and theoretically, the L.D.C have a slightly lower energy-gap value compared to the P.C sample. The films are discussed below by CIS and XPS to investigate the phenomena that occur at the semiconductor-bulk and surface levels and their relation to the strong dual-sensing behavior of the L.D.C sample.

3.4. Complex impedance spectroscopy

The conductance and capacitance variations with frequency strongly depend on the form and distribution of trap-states, which in turn depend on the amount and type of doping agent, gas exposure, and

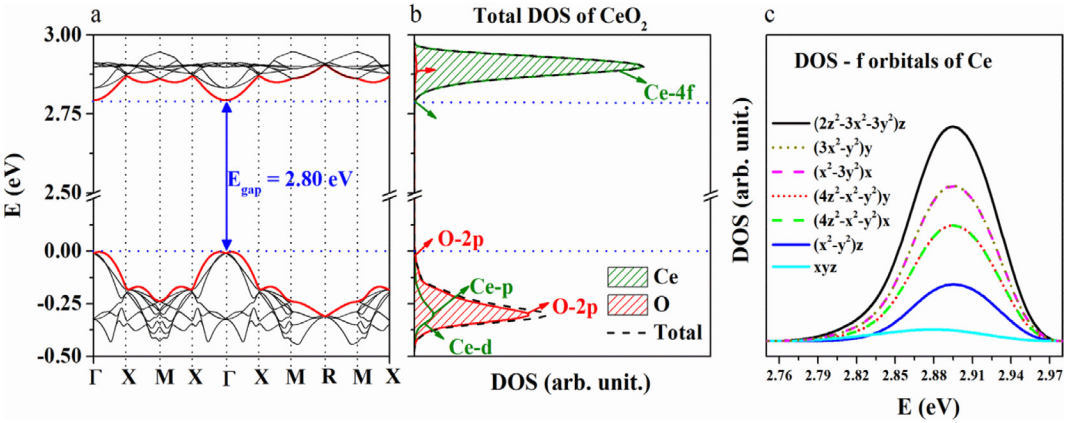

Fig. 4. (a) Band structure of CeO_2 model, (b) density of states projected in over Ce and O, and total atoms, (c) density of states for f orbitals.

temperature, and therefore demand specific studies for each case. Our samples particularly depicted only deep bulk-trap effects on the total electrical capacitance with no changes regarding grain boundaries (C_{GB}) because a mild band-bending should be expected for samples with a relatively great distance in between $E_c - E_F$ at approximately 3 eV. Therefore, the electrical conduction phenomena of the P.C and L.D.C particles can be related to the transient $4f^1$ electrons that migrate by an activated hopping mechanism of polarons intrinsically created after the reduction of Ce(IV) to Ce(III) which is more energetically favorable in P.C [67]. Only the L.D.C-based film exhibited a significant color change. This was likely associated with electrons that are promoted from the oxygen 2p states to lanthanum 3d states through the absorption of energy along with a facile reduction of Ce(IV) to Ce(III) owing to itinerant 4f electrons, interpreted as distortion processes of [CeO_8] clusters [24]. This sample was used for impedance measurements.

Fig. 6(a) shows the Nyquist Plot (imaginary vs real part of complex impedance) for the L.D.C film under distinct gaseous atmospheres (10^{-3} mmHg of vacuum, and 50 mmHg of synthetic air and CO) at 673 K (chosen because of the color change, that occurred at 653 K).

The resultant spectrum was characterized by the presence of compressed semicircle arcs under exposure to $CO_{(g)}$, vacuum, and air, with a significant decrease of $R_s(\Omega)$ in the presence of CO in comparison to vacuum and air. Regarding sensing behavior, the interaction between a gaseous species and a film surface plays a crucial role and can be separated into two steps:

(1) adsorption of oxygen atoms onto the surface owing to the contact with the surrounding environment resulting in the formation of distinct oxygen species(O_2(ads) and O_2^- for T < 423 K or O^- and O^{2-} species for T > 423 K) [68] followed by
(2) reaction of the adsorbed species with the target gas (CO) forming CO_2 along with electrons injected towards the conduction band of the semiconductor (4f states for CeO_2).

An increase in resistivity of the film was observed as a consequence of lanthanum doping [see Fig. 6 of Ref. [24] at t = 0). The energy difference between the conduction band and the Fermi level ($E_c - E_F$) increases because of the modification with La(III), with a consequent decrease in the number of available electrons for conduction and increase the initial electrical resistance of the L.D.C sample. However, exposure to a reducing atmosphere (CO gas) at 673 K provided energy to a great number of electrons that were easily available for conduction, thereby decreasing the sample electrical resistance. This behavior is clearly shown in Fig. 6(b) where the L.D.C sample exposed to CO had resistance values below the air and vacuum atmospheres for the entire frequency range.

Otherwise, oxygen diffusion towards a bulk annihilates oxygen vacancies and thus increases the sample resistivity as shown in Fig. 6(a) where samples were exposed to an air atmosphere. Compared to a reducing atmosphere, the semicircle diameter of the sample increased when exposed to air (oxidizing atmosphere). This phenomenon would be detectable in the capacitance (C_p) changes at high frequencies if there was band bending as in other oxides. However, the results of Fig. 6(c) do not support the above interpretation, as the capacitance at high frequencies did not change under distinct atmospheres and was in accordance with the expected values for bulk CeO_2 doped films, indicating a flat band at the surface. At very low frequencies, all the capacitances show a similar behavior, with a magnitude of 10^{-9} F, which is attributed to the trapping of charge carriers within structural defects [69–72].

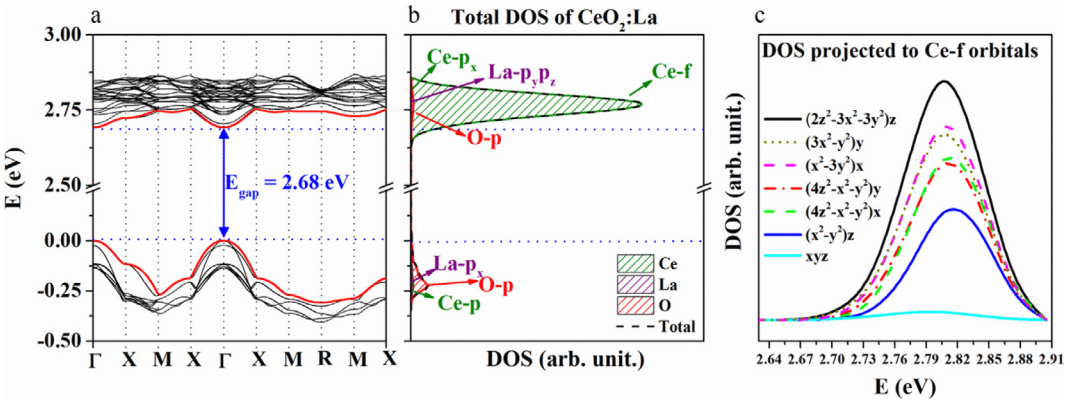

Fig. 5. (a) Band structure of CeO_2-La model, (b) density of states projected in over Ce, O, La and total atoms, (c) density of states for f orbitals.

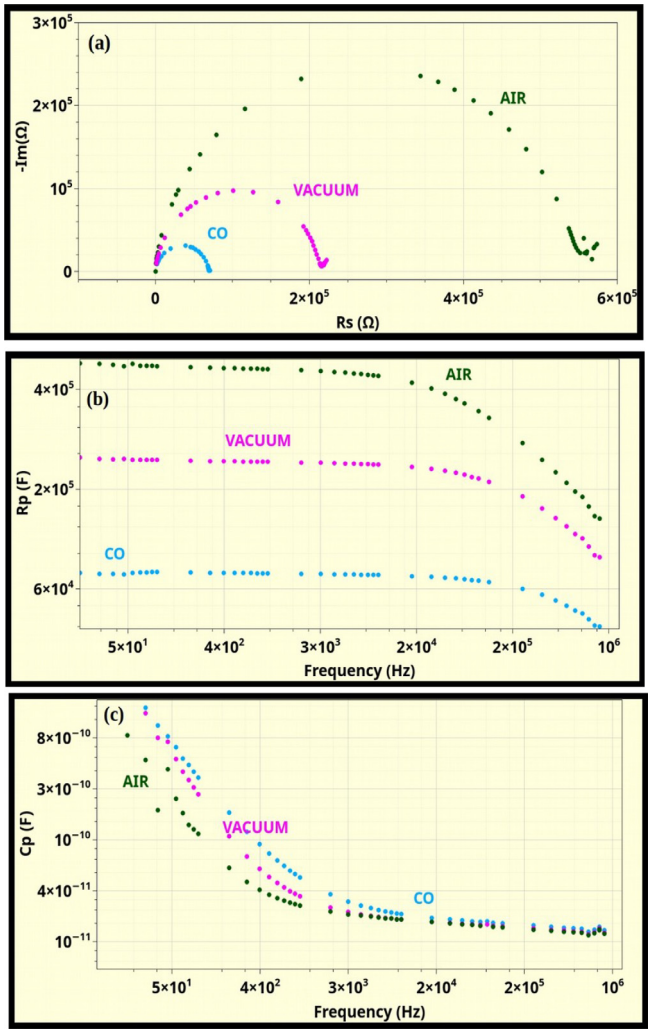

Fig. 6. (a) Nyquist plot, (b) Rp × f (Hz) and (c) Cp × f (Hz) for the L.D.C sample measured at 673 K under vacuum, air and CO atmospheres from 20 Hz to 1 MHz.

3.5. X-ray photoemission spectroscopy

The local binding structures of the samples were investigated by XPS. Fig. 7 shows the survey spectra for the P.C and L.D.C samples before and after $CO_{(g)}$ treatment at 673 K.

The survey showed that carbon, ceria, and oxygen atoms were present on the P.C film surface before and after CO treatment along, while expected lanthanum atoms were present on the L.D.C film depicting a similar increase in the atomic percentage (at. %) of C 1 s along with a reduction of Ce 3d for both samples after CO exposure.

For a more in-depth analysis, core-level spectra were made for the C 1 s and O 1 s species as shown in Fig. 8a and b, respectively. High-resolution analyses were performed for the core-level Ce 3d species (Fig. 8c), once the used excitation source didn't have an intense valence-band Ce-4f photoemission [73]. Therefore, further studies are required using resonant photoelectron spectroscopy using photon energies near 120 eV [74,75], to elucidate the relative concentration of the Ce^{3+}/Ce^{4+} oxidation states along the film surface.

The C 1s spectra exhibited no significant difference between the P.C to the L.D.C samples, depicted binding energy peaks of C—C and C—H (~284.5 eV), C—O (~286 eV), C═O (~288 eV), and O—C═O (~290 eV) species. The relative intensities of the C-O-type species were reduced after CO exposure because of the high surface reactivity of the ceria samples.

The O 1s spectra of the samples had present a slight difference in peak forms, which were deconvoluted to obtain additional information. These results indicate that the oxygen bonded to carbon was likely related to the carbonate and carbon dioxide (~531–533 eV) species and the hydroxyl and surface defects (~530 eV); oxygen also bonded to the lattice (~529 eV). It can be seen that the high binding-energy shoulders shifted because of the modification with lanthanum and the exposure to CO. Praline et al. [76] attributed these features to hydroxyl or some hydroxyl-containing oxide rather than to physisorbed oxygen. Laachir et al. [77] attributed these peaks to the emissions from the hydroxyl and carbonate species. For our samples, the C 1s emission didn't increase with the addition of lanthanum, or with exposure to CO; therefore, one can conclude that the shoulder unlikely came from the carbonate species once they were mostly eliminated after heat treatment at 653 K for 2 h.

The ratio of the O1s peaks related to structural defects and the peaks of the crystalline lattice are listed in Table 3. It is clear that the defective oxygen species of the L.D.C increased by approximately 8% compared to that of the P.C sample before and after exposure to CO, because of the structural modification with La(III). In the pure CeO_2 system, the reduction of Ce(IV) → Ce(III) was the result of the formation of oxygen vacancies that released electrons, transferred to their neighboring Ce(IV) cations, as shown in Eqs. (6) and (7) [41]:

$$O^{2-} \rightarrow 1/2\ O_{2(g)} + 2e' \quad (6)$$

$$Ce^{4+} + e' \rightarrow Ce^{3+} \quad (7)$$

It is evident that the deconvoluted Ce (3d) spectrum was relatively complex because of the presence of mixed Ce^{3+} and Ce^{4+} oxidation

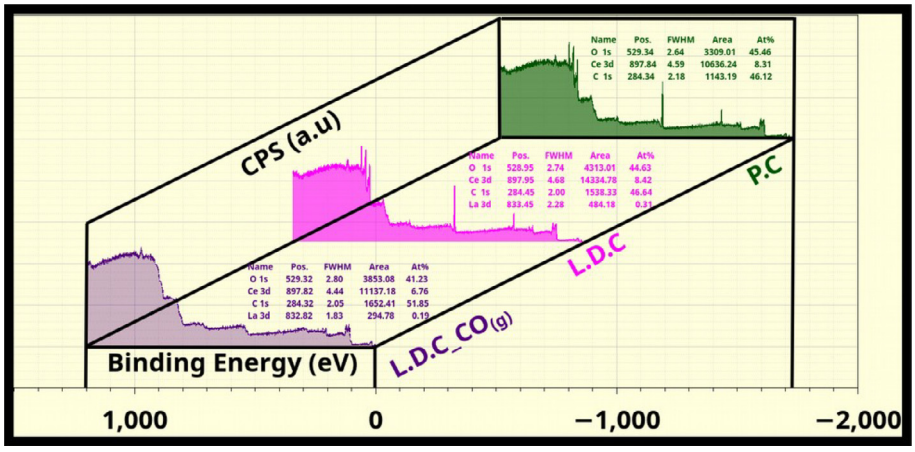

Fig. 7. XPS survey of P.C and L.D.C samples before and after CO exposure.

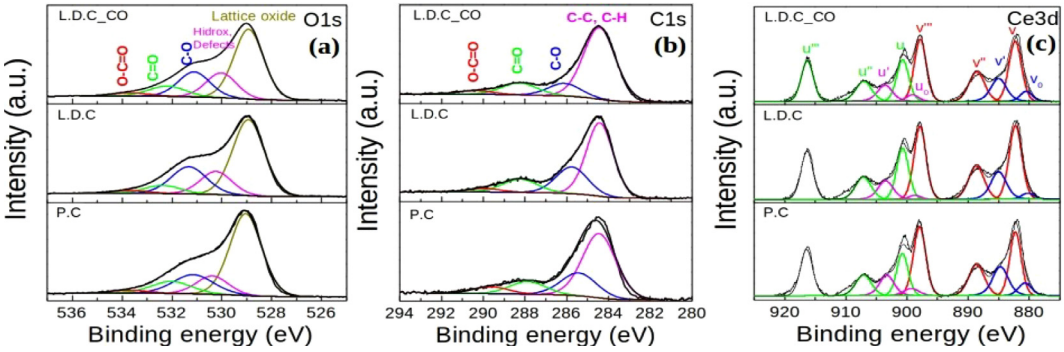

Fig. 8. XPS analyses of (a) O 1s, (b) C 1s and (c) Ce 3d species for the P.C and L.D.C samples before and after CO exposure.

Table 3
Analysis of the ratio of O1s of the defects of the crystalline lattice, and the relative concentration of surface Ce^{3+} species.

Sample	O_{defect} *Area*	$O_{lattice}$ *Area*	$O_{defect}/O_{lattice}$ *Ratio*	Ce^{3+} *%*
P.C	20,423	91,066	0.22	23.88
L.D.C	34,045	112,214	0.30	18.58
L.D.C_CO	35,127	96,534	0.36	20.42

states as evidenced by the spin-orbit multiplets that give rise to 10 distinct peaks.

The spectra were adjusted without constraints using multiple Gaussian profiles. The FWHM varied between 2.2 and 3.0 eV with a peak-position accuracy of ± 0.1 eV. The fitted peaks denoted as v and u refer to a set of multiplets regarding the spin-orbit coupling of $3d_{5/2}$ and $3d_{3/2}$, respectively. The doublets were separated by 18.5–18.6 eV. The peaks named as v_0, v′, u_0, and u′ refer to Ce in the oxidation state +3 [78,79], and v, v″, v‴, u, u″ and u‴ to Ce^{4+}. In particular, v, v″, and v‴ can be attributed to CeO_2, while v and v″ are likely assigned to a mixture of Ce $3d^94f^2$ – O $2p^4$ and Ce $3d^94f^1$ – O $2p^5$ configurations, and v‴ is a pure Ce $3d^94f^0$ – O $2p^6$ final state. The peak close to 916 eV (u‴) is a clear indicator of Ce(IV) once it has not superposed with any of the Ce(III) lines corresponding to the unscreened Ce-$3d_{3/2}$ final state of Ce^{4+} [80]. However, one cannot trace a linear dependence between the Ce^{4+} concentration and u‴ intensities [81]. However, v_0 and v′ are the result of a mixture of Ce $3d^94f^2$ – O $2p^4$ and Ce $3d^94f^1$ – O $2p^5$ configurations in Ce_2O_3-like structures [82,83]. The u structures can be explained in the same way owing to the Ce$3d_{3/2}$ level. These additional peaks resulted from the so-called “shake-down” states where electrons are transferred from the O 2p level to an excited Ce 4f state [84,85].

Using the relative areas of the components belonging to the corresponding oxidation states ($Area_{Ce^{3+}}$ and $Area_{Ce^{4+}}$), the relative concentration of Ce^{3+} (Table 3) was determined as:

$$\%Ce^{3+} = [Area_{Ce^{3+}} (Area_{Ce^{3+}} + Area_{Ce^{4+}})]x100\% \quad (8)$$

As shown in Table 3 (1st and 2nd row), an increase of 8% in the proportion of defective to lattice-oxygen species as a consequence of La-doping was observed, likely ascribed to the creation of oxygen vacancies. This result can be depicted as 22% of the P.C sample having vacant oxygen sites in its structure against 30% for the L.D.C sample. The decrease of more than 5% in the Ce^{3+} surface content after doping with lanthanum was consistent with the increase of bulk singly ionized oxygen species detected with EPR spectroscopy.

We must consider the equilibrium between the ordered and disordered $[CeO_8]$ clusters, with their resonance being represented as:

$$[CeO_8]_o^x \leftrightarrow [CeO_8]_d^x \quad (9)$$

Then, we can consider the intrinsic generation of the following clusters:

$$[CeO_8]_o^x + [CeO_8]_d^x \rightarrow [CeO_8]_o' + [CeO_7.V_o^{\cdot}] + \tfrac{1}{2}O_2 \quad (10)$$

$$[CeO_8]_o^x + [CeO_7.V_o^{\cdot}] \rightarrow [CeO_8]_o' + [CeO_7.V_o^{\cdot\cdot}] \quad (11)$$

$$[CeO_8]_o^x + [CeO_7.V_o^x] \rightarrow [CeO_8]_o' + [CeO_7.V_o^{\cdot}] \quad (12)$$

$$[CeO_7.V_O^x] + [CeO_7.V_O^{\cdot}] \rightarrow [CeO_7.V_O^x]_o' + [CeO_7.V_O^{\cdot\cdot}] \quad (13)$$

In air atmosphere, the interaction of oxygen species with these clusters can likely be considered as:

$$[CeO_7.V_o^x] + O_2 \rightarrow [CeO_7.V_o^x]\cdots O_{2\ (ads)} \quad (14)$$

$$[CeO_7.V_o^{\cdot}] + O_2 \rightarrow [CeO_7.V_o^{\cdot}]\cdots O_{2(ads)} \quad (15)$$

$$[CeO_7.V_o^{\cdot\cdot}] + O_2 \rightarrow [CeO_7.V_o^{\cdot\cdot}]\cdots O_{2(ads)} \quad (16)$$

We also must consider that different oxygen species can be formed depending on the working temperature [86]. For CeO_2 clusters, we can rewrite the Eqs. (14) and (15) as:

$$[CeO_7.V_o^x]\ldots O_{2(ads)} \rightarrow [CeO_7.V_o^{\cdot}]\cdots O_2'_{(ads)} \quad (17)$$

$$[CeO_7.V_o^{\cdot}]\ldots O_{2(ads)} \rightarrow [CeO_7.V_o^{\cdot\cdot}]\cdots O_{2(ads)} \text{ for } (T > 573\ K) \quad (18)$$

Eqs. (17) and (18) lead to the amount of ionized oxygen species adsorbed onto the CeO_2 surface; we could also have used the steps in which an electron is transferred from the Ce^{+3} to the oxygen adsorbed onto the surface. This possible transfer can decrease the number of electron in 4f states and reduce the hopping electrical conduction.

$$[CeO_7.V_o^x]\cdots O_{2(ads)} + [CeO_8]_o' \rightarrow [CeO_7.V_o^x]\cdots O_2' + [CeO_8]_o^x \quad (19)$$

$$[CeO_7.V_o^{\cdot}]\cdots O_{2(ads)} + [CeO_8]_o' \rightarrow [CeO_7.V_o^{\cdot}]\cdots O_2' + [CeO_8]_o^x \quad (20)$$

$$[CeO_7.V_o^{\cdot\cdot}]\cdots O_{2(ads)} + [CeO_8]_o' \rightarrow [CeO_7.V_o^{\cdot\cdot}]\cdots O_2' + [CeO_8]_o^x \quad (21)$$

After exposure to CO, one can assume that part of the available Ce^{4+} species in the L.D.C sample reacted at the surface once the Ce(III) increased by almost 2%, and the defective ($V_O^{\cdot}$) oxygen species increased by 6%. Once the exposure to $CO_{(g)}$ at 653 K had raised the amount of oxygen vacant sites for both cases, the interaction of the gas with the film surface of the P.C and L.D.C samples can be established through the reaction with adsorbed oxygen species represented by Eqs. (22) and (23), normally used to explain semiconductors reaction with $CO_{(g)}$ [87,88].

$$CO + O^- \rightarrow CO_2 + V_O^{\cdot} + e' \quad (22)$$

$$CO + O^{2-} \rightarrow CO_2 + V_O^{\cdot\cdot} + 2e' \quad (23)$$

At temperatures greater than 450 K, CO reacts with the adsorbed oxygen species on the CeO_2 surface according to the following equations:

$$2CO + O_{2(ads)}^- \rightarrow 2CO_2 + e^- \ (T < 373\ K), \quad (24)$$

$$CO + O^- \rightarrow CO_2 + e^- \ (373\ K < T < 573\ K), \quad (25)$$

$$2CO + 2O_{2(ads)}^{-} \rightarrow 2CO_2 + 2e^{-} + O_2(T > 573\ K), \quad (26)$$

When samples were previously exposed to an oxygen atmosphere and later to a CO atmosphere, Eq. (26) can be expressed as:

$$[CeO_7.V_o^{x}] + [CeO_7.V_o^{\bullet}]\cdots O_2 \rightarrow [CeO_7.V_o^{\bullet}]\cdots O_2^{'} + [CeO_7.V_o^{\bullet}] \quad (27)$$

$$[CeO_7.V_o^{\bullet}]\cdots O_2^{'} + CO \rightarrow [CeO_7.V_o^{\bullet}]\cdots \acute{O}\cdots CO_2 \quad (28)$$

$$[CeO_7.V_o^{\bullet}]\cdots \acute{O}\cdots CO_{2(ads)} \rightarrow [CeO_7.V_o^{x}] + CO_2 + \tfrac{1}{2}O_2 \quad (29)$$

where, the electrons situated in the $O_2^{'}$ species adsorbed onto the surface, returned to the bulk, reduced the cluster system from $[CeO_7.V_o^{\bullet}]$ to $[CeO_7.V_o^{x}]$, and increased the electrical conduction. However, if the sample had been previously exposed to a vacuum atmosphere, then we must consider the reaction between CO and the oxygen clusters as follows.

$$2[CeO_8]_o^{x}\cdots[CeO_8]_d^{x}\cdots CO \rightarrow [CeO_8]_o{'}\cdots[CeO_7.V_o^{\bullet\bullet}]\cdots[CeO_8]_o{'} + CO_2 \quad (30)$$

From the previous equations, we can observe that when CO reacts at the surface (with oxygen adsorbed or with the lattice oxygen) two electrons are available for the 4f states, thus increasing the number of Ce^{3+} species ($[CeO_8]_o{'}$) on the right side of the equation. The proposed cluster $[CeO_8]_o{'}\cdots[CeO_7.V_O^{\bullet\bullet}]\cdots[CeO_8]_o{'}$ was previously suggested in studies using a positron annihilation lifetime spectroscopy (PALS) technique [89,90].

Exposure to $CO_{(g)}$ caused an increase of almost 2% in the amount of Ce(III) species on the surface. Note that pure cerium dioxide virtually did not undergo any color change, while the lanthanum-doped film had reversibly and almost instantaneously (~0.3 s) done so [24]. Considering the presence of localized 4f electrons that acquired energy through the exposure of $CO_{(g)}$ at 653 K, within a cubic symmetry with a mean crystallite size of more than 10 nm, the electrical transport can be easily ascribed to the hopping process in which electrons hop rather than tunnel from one atom/molecule to another [91]. The interaction of electrons and phonons in the lattice site may lead to self-trapping, in which the electrons polarize their neighboring molecules and become trapped in self-induced potential wells, because of the polarization field generated by the moving electrons carried through the lattice. This combination can be considered as a quasi-particle generally referred to as a polaron [92,93].

The previously reported process of luminescence visible to the naked eye [24] corresponds to the de-excitation of those excited atoms or molecules (or the annihilation of excitons through recombination) by re-emission of the absorbed energy as light [94]. Therefore, the following structural aspects of the P.C sample can be taken into consideration when using the Eqs. (9)–(13): The presence of Ce^{4+} species is represented using $[CeO_8]^{x}$, $[CeO_7.V_o^{x}]$, and $[CeO_7.V_O^{\cdot}]$ for neutral and paramagnetic clusters and $[CeO_7.V_O^{\bullet\bullet}]$ for non-paramagnetic clusters. The presence of Ce^{3+} species is represented by the $[CeO_8]_o{'}$ cluster, while the formation of a cluster with two paramagnetic vacancies, also likely responsible for the paramagnetic effect, can be represented by $[CeO_7.V_O^{\cdot} - LaO_7.V_O^{\cdot}]$.

For the L.D.C sample, we also have to consider the presence of lanthanum atoms that form complex clusters of defects that can be represented as.

$$[LaO_8]_o^{x}\cdots[LaO_7.V_O^{x}] \rightarrow [LaO_8]_o{'}\ldots[LaO_7.V_O^{\cdot}] \quad (31)$$

$$[LaO_8]_o^{x}\cdots[CeO_7.V_O^{x}] \rightarrow [LaO_8]_o{'}\ldots[CeO_7.V_O^{\cdot}] \quad (32)$$

$$[CeO_8]_o^{x}\cdots[LaO_7.V_O^{x}] \rightarrow [CeO_8]_o^{x}\ldots[LaO_7.V_O^{\cdot}]' \quad (33)$$

$$[CeO_8.]_o{'} + [LaO_7.V_o^{\bullet}] \rightarrow [CeO_7.V_o^{\bullet}] + [LaO_8.]_o{'} \quad (34)$$

$$[CeO_8.]_o{'} + [LaO_8]^{x} + [LaO_7.V_o^{x}] \leftrightarrow [CeO_8]_o^{x} + [LaO_7.V_o^{\bullet}]' + [LaO_8]_o{'} \quad (35)$$

Using the previous results considering the positron annihilation lifetime spectroscopy [89] technique, these equations can be written as.

$$[LaO_8]_o^{x} + [LaO_7.V_o^{x}] \rightarrow [LaO_7.V_o^{\bullet}]\ldots[LaO_8]_o{'} \quad (36)$$

$$[LaO_8]_o^{x} + [LaO_7.V_o^{\bullet}]' \rightarrow [LaO_7.V_o^{\bullet\bullet}]'\ldots[LaO_8]_o{'} \quad (37)$$

Worth to mention that these equations are only bi-dimensional representations and that a volumetric three-dimensional perspective should be taken into consideration. Therefore, the observed free charges could likely be localized in any of the rare-earth elements neighboring the oxygen-vacant sites.

We can also consider a doubly-ionized oxygen vacancy formation during this process, which would lead to a non electrical resistance change written as.

$$[LaO_8.]_o{'}\cdots[CeO_7.V_o^{\bullet}]\cdots[LaO_8]_o^{x} \rightarrow [LaO_8]_o{'}\cdots[CeO_7.V_o^{\bullet\bullet}]\cdots[LaO_8]_o{'} \quad (38)$$

Eq. (38) represents the increase in the EPR signal when samples are doped along with an increase in the number of defective clusters after La addition and a decrease of Ce^{3+} species. To clarify, with the introduction of quasi-Fermi levels (4f states) for trapped electron and holes, defect states in the forbidden energy gap may act as electron or hole traps depending on their states of occupancy, and the trapping states can be classified as shallow or deep traps. The electron states involved in the reaction process decrease with an increase in energy from the quasi-Fermi level for trapped electrons up to the edge of the conduction band or with a decrease in energy from the quasi-Fermi level for trapped holes down to the top of the valence band. Free carriers falling into one of these states will then be re-emitted with high probability back into the band from which they came. The temperature for establishing the degree of occupancy will determine whether a trap acts as a shallow trap. Reasonably, we use this definition of a shallow trap state as a "statistical" one in contrast to the distinction between the shallow and deep trap states provided by physical arguments. Shallow traps are characterized by a very small ionization energy that in the order of phonon energies. Deep traps have ionization energies many times that of the phonon, and consequently, the capture of a free carrier may involve multiphonon transitions. At temperatures above several degrees Kelvin, shallow trap states are empty and both definitions of shallow traps are identical. However, at the elevated temperatures in our case, deep trap states may turn into "statistically" shallow traps, forming very complex defective clusters.

4. Conclusion

The XRD results confirmed the effectiveness of the MAH technique in obtaining pure and lanthanum-doped ceria polycrystalline nanopowders within low reaction times and temperatures once the obtained samples were well-indexed to a pure fluorite-type cubic structure (space group: *Fm3m*) with a theoretical lattice parameter of 5.411 Å.

The EPR result with the highly symmetric pattern typical of materials with total spin (S) = ½, confirmed the increase in the content of paramagnetic species after Lanthanum modification, while the UV–Vis spectroscopy showed a narrowing of 0.2 eV in the energy-gap between the Fermi level and the valence band because of this doping. The theoretical results corroborate the band gap energy reduction, the predominance of the 4f orbitals in the conduction band and the unfolding of the *f* orbitals levels with doping.

The CIS measurements confirmed the electrical response of the La-doped system against a CO atmosphere, showing its potential as a gas-sensor material. The CIS study also revealed an increase in total electrical resistance in response to air atmosphere exposure because of the oxygen adsorption at the grain surfaces and diffusion into the grains which annihilated oxygen vacancies and thereby generated a decrease in conductance. For the reducing atmosphere, with CO exposure, the total resistance of the system decreased, and this phenomenon was direct proof of an increase of the oxygen vacancies along with the

consequent reduction of the Ce(IV) → Ce(III) reaction.

In conclusion, the XPS spectra of pure and lanthanum-doped CeO_2 were obtained, and detailed analysis showed that the addition of a relatively small quantity of La^{3+} along with the exposure to a reducing atmosphere such as CO resulted in the following significant events: (I) the promotion of the conversion of some Ce^{3+} into Ce^{4+} and vice-versa, (ii) the narrowing of the "effective band-gap" in 0.2 eV, and (iii) the creation of singly ionized oxygen vacancy species that changed the total electrical resistance because of the strong contribution of the 4f orbitals as shown by theoretical simulations. This conclusion is a good indication that the dual behavior of the La-doped CeO_2 film originates from intrinsic defects and charge transfer after a certain degree of structural disorder arising from the contribution of different intermediary energy levels within the band-gap as a result of the lanthanum addition.

CRediT authorship contribution statement

Leandro Silva Rosa Rocha: Conceptualization, Methodology, Validation, Formal analysis, Investigation, Writing - original draft, Writing - review & editing, Visualization. **Rafael Ciola Amoresi:** Methodology, Software, Validation, Formal analysis, Investigation, Writing - original draft, Visualization. **Thiago Marinho Duarte:** Methodology, Software, Validation, Formal analysis, Investigation, Writing - original draft, Visualization. **Naiara Letícia Marana:** Methodology, Software, Validation, Formal analysis, Investigation, Writing - original draft, Visualization. **Julio Ricardo Sambrano:** Methodology, Software, Validation, Formal analysis, Investigation, Writing - original draft, Visualization. **Celso Manuel Aldao:** Methodology, Software, Validation, Formal analysis, Investigation, Writing - original draft, Visualization. **Alexandre Zirpoli Simões:** Conceptualization, Methodology, Software, Validation, Formal analysis, Investigation, Writing - original draft, Visualization, Supervision. **Miguel Adolfo Ponce:** Methodology, Software, Validation, Formal analysis, Investigation, Writing - original draft, Visualization. **Elson Longo:** Methodology, Software, Validation, Formal analysis, Investigation, Resources, Writing - original draft, Visualization, Supervision, Funding acquisition.

Data availability

The raw as well as processed data required to reproduce these findings are available to download from https://data.mendeley.com/datasets/xnxv4r8js6/2.

Declaration of Competing Interest

The authors declare that they have no known competing financial interests or personal relationships that could have appeared to influence the work reported in this paper.

Acknowledgements

The authors thank the following Brazilian agencies for their financial support of this research project: "Coordenação de Aperfeiçoamento de Pessoal de Nível Superior" - Brazil (CAPES) - Finance Code 001, the National Council for Scientific and Technological Development (CNPq), and "Fundação de Amparo à Pesquisa do Estado de São Paulo" (FAPESP), grants n° 13/07296-2 (CEPID), 2017/19143-7, 2016/25500-4, and 2018/20590-0. We also thank Dr. Ednan Joanni (CTI Renato Archer, Campinas, Brazil) for the provided substrates, Embrapa for the EPR measurements and the Modeling and Molecular Simulations Group, São Paulo State University, UNESP, Bauru for theoretical studies.

Appendix A. Supplementary material

Supplementary data to this article can be found online at https://doi.org/10.1016/j.apsusc.2019.145216.

References

[1] Z.K. Ghouri, N.A.M. Barakat, H.Y. Kim, et al., Nano-engineered ZnO/CeO2dots@CNFs for fuel cell application, Arab. J. Chem. 9 (2016) 219–228, https://doi.org/10.1016/j.arabjc.2015.05.024.
[2] L. Li, B. Zhu, J. Zhang, et al., Electrical properties of nanocube CeO2in advanced solid oxide fuel cells, Int. J. Hydrogen Energy 43 (2018) 12909–12916, https://doi.org/10.1016/j.ijhydene.2018.05.120.
[3] A.A.A. da Silva, N. Bion, F. Epron, et al., Effect of the type of ceria dopant on the performance of Ni/CeO2SOFC anode for ethanol internal reforming, Appl. Catal. B Environ. 206 (2017) 626–641, https://doi.org/10.1016/j.apcatb.2017.01.069.
[4] X. Zheng, S. Huang, D. Yang, et al., Synthesis of X-architecture CeO2 for the photodegradation of methylene blue under UV-light irradiation, J. Alloys Compd. 705 (2017) 131–137, https://doi.org/10.1016/j.jallcom.2017.02.110.
[5] J. Zou, B. Yu, S. Zhang, et al., Hydrogen production from ethanol over Ir/CeO2 catalyst: effect of the calcination temperature, Fuel 159 (2015) 741–750, https://doi.org/10.1016/j.fuel.2015.07.040.
[6] H. Liu, Z. Feng, X. Huang, et al., Study on purification and application of novel precipitant for ceria-based polishing powder, J. Rare Earths 31 (2013) 174–179, https://doi.org/10.1016/S1002-0721(12)60254-3.
[7] A. Umar, R. Kumar, M.S. Akhtar, et al., Growth and properties of well-crystalline cerium oxide (CeO2) nanoflakes for environmental and sensor applications, J. Colloid Interface Sci. 454 (2015) 61–68, https://doi.org/10.1016/j.jcis.2015.04.055.
[8] J. Hu, C. Zou, Y. Su, et al., Light-assisted recovery for a highly-sensitive NO2 sensor based on RGO-CeO2 hybrids, Sensors Actuat. B Chem. 270 (2018) 119–129, https://doi.org/10.1016/j.snb.2018.05.027.
[9] R. You, T. Wang, H. Yu, et al., Mixed-potential-type NO2 sensors based on stabilized zirconia and CeO2-B2O3 (B = Fe, Cr) binary nanocomposites sensing electrodes, Sensors Actuat. B Chem. 266 (2018) 793–804, https://doi.org/10.1016/j.snb.2018.03.140.
[10] X. Yang, X. Hao, T. Liu, et al., CeO2-based mixed potential type acetone sensor using La1-xSrxCoO3 sensing electrode, Sensors Actuat. B Chem. 269 (2018) 118–126, https://doi.org/10.1016/j.snb.2018.04.160.
[11] C. Liu, H. Tai, P. Zhang, et al., A high-performance flexible gas sensor based on self-assembled PANI-CeO2 nanocomposite thin film for trace-level NH3 detection at room temperature, Sensors Actuat. B Chem. 261 (2018) 587–597, https://doi.org/10.1016/j.snb.2017.12.022.
[12] J.A. Hoskins, Carbon monoxide: the unnoticed poison of the 21st century, Indoor Built Environ. 8 (1999) 154–155, https://doi.org/10.1159/000024630.
[13] J.D. Roderique, C.S. Josef, M.J. Feldman, B.D. Spiess, A modern literature review of carbon monoxide poisoning theories, therapies, and potential targets for therapy advancement, Toxicology 334 (2015) 45–58, https://doi.org/10.1016/j.tox.2015.05.004.
[14] D. Stearns, K. Sircar, National unintentional carbon monoxide poisoning estimates using hospitalization and emergency department data, Am. J. Emerg. Med. (2018), https://doi.org/10.1016/j.ajem.2018.06.002.
[15] H. Hojo, T. Mizoguchi, H. Ohta, et al., Atomic structure of a CeO2 grain boundary: the role of oxygen vacancies, Nano Lett. 10 (2010) 4668–4672, https://doi.org/10.1021/nl1029336.
[16] P.R.L. Keating, D.O. Scanlon, G.W. Watson, The nature of oxygen states on the surfaces of CeO2 and La-doped CeO2, Chem. Phys. Lett. 608 (2014) 239–243, https://doi.org/10.1016/j.cplett.2014.05.094.
[17] H.L. Tuller, A.S. Nowick, Small polaron electron transport in reduced CeO2 single crystals, J. Phys. Chem. Solids 38 (1977) 859–867, https://doi.org/10.1016/0022-3697(77)90124-X.
[18] B. Choudhury, A. Choudhury, Ce 3+ and oxygen vacancy mediated tuning of structural and optical properties of CeO 2 nanoparticles, Mater. Chem. Phys. 131 (2012) 666–671, https://doi.org/10.1016/j.matchemphys.2011.10.032.
[19] P. Dutta, S. Pal, M.S. Seehra, et al., Concentration of Ce3+ and oxygen vacancies in cerium oxide nanoparticles, Chem. Mater. 18 (2006) 5144–5146, https://doi.org/10.1021/cm061580n.
[20] E.A. Shaw, A.P. Walker, T. Rayment, R.M. Lambert, Methanol synthesis activity of Au/CeO2 catalysts derived from a CeAu2 alloy precursor: do schottky barriers matter? J. Catal. 134 (1992) 747–750, https://doi.org/10.1016/0021-9517(92)90359-P.
[21] P. Gao, Z. Wang, W. Fu, et al., In situ TEM studies of oxygen vacancy migration for electrically induced resistance change effect in cerium oxides, Micron 41 (2010) 301–305, https://doi.org/10.1016/j.micron.2009.11.010.
[22] D. Schmeißer, G. Appel, O. Böhme, et al., Nanoparticles and polarons: active centers in thin film sensor devices, Sensors Actuat. B Chem. 70 (2000) 131–138, https://doi.org/10.1016/S0925-4005(00)00582-7.
[23] E. Wuilloud, B. Delley, W.-D. Schneider, Y. Baer, Spectroscopic evidence for localized and extended f-symmetry states in CeO2, Phys. Rev. Lett. 53 (1984) 202–205, https://doi.org/10.1103/PhysRevLett. 53.202.
[24] L.S.R. Rocha, M. Cilense, M.A. Ponce, et al., Novel gas sensor with dual response under CO(g) exposure: optical and electrical stimuli, Phys. B Condens. Matter 536 (2018) 280–288, https://doi.org/10.1016/j.physb.2017.10.083.
[25] L. Kumar, P. Kumar, A. Narayan, M. Kar, Rietveld analysis of XRD patterns of

different sizes of nanocrystalline cobalt ferrite, Int. Nano Lett. 3 (2013) 8, https://doi.org/10.1186/2228-5326-3-8.
[26] A.R. Bushroa, R.G. Rahbari, H.H. Masjuki, M.R. Muhamad, Approximation of crystallite size and microstrain via XRD line broadening analysis in TiSiN thin films, Vacuum 86 (2012) 1107–1112, https://doi.org/10.1016/j.vacuum.2011.10.011.
[27] Y. Zhao, J. Zhang, Microstrain and grain-size analysis from diffraction peak width and graphical derivation of high-pressure thermomechanics, J. Appl. Crystallogr. 41 (2008) 1095–1108, https://doi.org/10.1107/S0021889808031762.
[28] A. Erba, J. Baima, I. Bush, et al., Large-scale condensed matter DFT simulations: performance and capabilities of the CRYSTAL code, J. Chem. Theory Comput. 13 (2017) 5019–5027, https://doi.org/10.1021/acs.jctc.7b00687.
[29] M. Corno, C. Busco, B. Civalleri, P. Ugliengo, Periodic ab initio study of structural and vibrational features of hexagonal hydroxyapatite Ca10(PO4)6(OH)2, Phys. Chem. Chem. Phys. 8 (2006) 2464–2472, https://doi.org/10.1039/B602419J.
[30] J. Graciani, A.M. Márquez, J.J. Plata, et al., Comparative study on the performance of hybrid DFT functionals in highly correlated oxides: the case of CeO2 and Ce2O3, J. Chem. Theory Comput. 7 (2011) 56–65, https://doi.org/10.1021/ct100430q.
[31] P.P. Ortega, L.S.R. Rocha, J.A. Cortés, et al., Towards carbon monoxide sensors based on europium doped cerium dioxide, Appl Surf Sci 464 (2019) 692–699, https://doi.org/10.1016/j.apsusc.2018.09.142.
[32] F. Schipani, M.A. Ponce, E. Joanni, et al., Study of the oxygen vacancies changes in SnO2 polycrystalline thick films using impedance and photoemission spectroscopies, J Appl Phys 116 (2014), https://doi.org/10.1063/1.4902150.
[33] Glycerin Producers' Association (1963) Physical properties of glycerine and its solutions. New York.
[34] K.I. Maslakov, Y.A. Teterin, A.J. Popel, et al., XPS study of ion irradiated and unirradiated CeO2 bulk and thin film samples, Appl. Surf. Sci. 448 (2018) 154–162, https://doi.org/10.1016/j.apsusc.2018.04.077.
[35] J.P. Holgado, R. Alvarez, G. Munuera, Study of CeO2 XPS spectra by factor analysis: reduction of CeO2, Appl. Surf. Sci. 161 (2000) 301–315, https://doi.org/10.1016/S0169-4332(99)00577-2.
[36] S. Deshpande, S. Patil, S.V. Kuchibhatla, S. Seal, Size dependency variation in lattice parameter and valency states in nanocrystalline cerium oxide, Appl. Phys. Lett. 87 (2005) 1–3, https://doi.org/10.1063/1.2061873.
[37] M. Hirano, M. Inagaki, Preparation of monodispersed cerium(iv) oxide particles by thermal hydrolysis: influence of the presence of urea and Gd doping on their morphology and growth, J. Mater. Chem. 10 (2000) 473–477, https://doi.org/10.1039/A907510K.
[38] K. Polychronopoulou, A.F. Zedan, M.S. Katsiotis, et al., Rapid microwave assisted sol-gel synthesis of CeO2 and CexSm1-xO2 nanoparticle catalysts for CO oxidation, J. Mol. Catal. A Chem. 428 (2016) 41–55, https://doi.org/10.1016/j.molcata.2016.11.039.
[39] T.R. Sahoo, M. Armandi, R. Arletti, et al., Pure and Fe-doped CeO 2 nanoparticles obtained by microwave assisted combustion synthesis: physico-chemical properties ruling their catalytic activity towards CO oxidation and soot combustion, Appl. Catal. B Environ. 211 (2017) 31–45, https://doi.org/10.1016/j.apcatb.2017.04.032.
[40] T.M.K. Thandavan, S.M.A. Gani, C.S. Wong, R.M. Nor, Evaluation of Williamson-Hall strain and stress distribution in ZnO nanowires prepared using aliphatic alcohol, J. Nondestruct. Eval. 34 (2015) 1–9, https://doi.org/10.1007/s10921-015-0286-8.
[41] K. Singh, K. Kumar, S. Srivastava, A. Chowdhury, Effect of rare-earth doping in CeO2 matrix: correlations with structure, catalytic and visible light photocatalytic properties, Ceram. Int. 43 (2017) 17041–17047, https://doi.org/10.1016/j.ceramint.2017.09.116.
[42] R.C. Deus, M. Cilense, C.R. Foschini, et al., Influence of mineralizer agents on the growth of crystalline CeO 2 nanospheres by the microwave-hydrothermal method, J. Alloys Compd. 550 (2013) 245–251, https://doi.org/10.1016/j.jallcom.2012.10.001.
[43] D.E. Motaung, G.H. Mhlongo, P.R. Makgwane, et al., Ultra-high sensitive and selective H2 gas sensor manifested by interface of n–n heterostructure of CeO2-SnO2 nanoparticles, Sensors Actuat. B Chem. 254 (2018) 984–995, https://doi.org/10.1016/j.snb.2017.07.093.
[44] P. Ratnasamy, D. Srinivas, C.V.V. Satyanarayana, et al., Influence of the support on the preferential oxidation of CO in hydrogen-rich steam reformates over the CuO–CeO2–ZrO2 system, J. Catal. 221 (2004) 455–465, https://doi.org/10.1016/j.jcat.2003.09.006.
[45] V.D. Araujo, W. Avansi, H.B. De Carvalho, et al., CeO2 nanoparticles synthesized by a microwave-assisted hydrothermal method: evolution from nanospheres to nanorods, CrystEngComm 14 (2012) 1150, https://doi.org/10.1039/c1ce06188g.
[46] B.M. Weckhuysen, R. Heidler, R.A. Schoonheydt, Electron spin Resonance spectroscopy, Mol Sieves 4 (2004) 295–335, https://doi.org/10.1007/b94238.
[47] R.M. Rakhmatullin, V.V. Pavlov, V.V. Semashko, EPR study of nanocrystalline CeO_2 exhibiting ferromagnetism at room temperature, Phys. Status Solidi 5 (2015), https://doi.org/10.1002/pssb.201552542.
[48] R.M. Rakhmatullin, I.N. Kurkin, V.V. Pavlov, V.V. Semashko, EPR, optical, and dielectric spectroscopy of Er-doped cerium dioxide nanoparticles, Phys. Status Solidi Basic Res. 251 (2014) 1545–1551, https://doi.org/10.1002/pssb.201451116.
[49] B.L. Bales, Correction for inhomogeneous line broadening in spin labels, II, J. Magn. Reson. 48 (1982) 418–430, https://doi.org/10.1016/0022-2364(82)90074-9.
[50] G. Casteleijn, J.J. Ten Bosch, J. Smidt, Error analysis of the determination of spin concentration with the electron spin resonance method, J. Appl. Phys. 39 (1968) 4375–4380, https://doi.org/10.1063/1.1656979.
[51] E. Abi-Aad, A. Bennani, J.-P. Bonnelle, A. Aboukais, Transition-metal ion dimers formed in CeO2: an EPR study, J. Chem. Soc. Faraday Trans. 91 (1995) 99–104, https://doi.org/10.1039/FT9959100099.
[52] E. Abi-aad, R. Bechara, J. Grimblot, A. Aboukais, Preparation and characterization of ceria under an oxidizing atmosphere. Thermal analysis, XPS, and EPR study, Chem. Mater. 5 (1993) 793–797, https://doi.org/10.1021/cm00030a013.
[53] C. Oliva, G. Termignone, F.P. Vatti, et al., Electron paramagnetic resonance spectra of CeO2 catalyst for CO oxidation, J. Mater. Sci. 31 (1996) 6333–6338, https://doi.org/10.1007/BF00354457.
[54] J.B. Wang, Y.-L. Tai, W.-P. Dow, T.-J. Huang, Study of ceria-supported nickel catalyst and effect of yttria doping on carbon dioxide reforming of methane, Appl. Catal. A Gen. 218 (2001) 69–79, https://doi.org/10.1016/S0926-860X(01)00620-2.
[55] R.W. Bierig, M.J. Weber, S.I. Warshaw, Paramagnetic resonance and relaxation of trivalent rare-earth ions in calcium fluoride II. Spin-lattice relaxation, Phys. Rev. 134 (1964) A1504–A1516, https://doi.org/10.1103/PhysRev.134.A1504.
[56] M.B. Kanoun, A.H. Reshak, N. Kanoun-Bouayed, S. Goumri-Said, Evidence of Coulomb correction and spinorbit coupling in rare-earth dioxides CeO2, PrO2 and TbO2: an ab initio study, J. Magn. Magn Mater 324 (2012).
[57] W. Wang, Q. Zhu, Q. Dai, X. Wang, Fe doped CeO 2 nanosheets for catalytic oxidation of 1, 2-dichloroethane: effect of preparation method, Chem. Eng. J. 307 (2017) 1037–1046, https://doi.org/10.1016/j.cej.2016.08.137.
[58] G. Ahuja, S. Sharma, G. Arora, Investigation of electronic structure of CeO2: first principles calculations, Int. J. Chem. Sci. 14 (2016) 1907–1917.
[59] H. Shi, T. Hussain, R. Ahuja, et al., Role of vacancies, light elements and rare-earth metals doping in, Nat. Publ. Gr. (2016) 1–8, https://doi.org/10.1038/srep31345.
[60] P.K. Sane, S. Tambat, S. Sontakke, P. Nemade, Visible light removal of reactive dyes using CeO2 synthesized by precipitation, J. Environ. Chem. Eng. 6 (2018) 4476–4489, https://doi.org/10.1016/j.jece.2018.06.046.
[61] D. Channei, P. Jannoey, A. Nakaruk, S. Phanichphant, Photocatalytic activity of Cu-doped cerium dioxide nanoparticles, Key Eng. Mater. 751 (2017) 801–806, https://doi.org/10.4028/www.scientific.net/KEM.751.801.
[62] X.F. Niu, Hydrothermal synthesis and optical properties of ellipsoid-like CeO2 nanostructures with rugged surface and many pores, J. Nano Res. 48 (2017) 95–103, https://doi.org/10.4028/www.scientific.net/JNanoR.48.95.
[63] U. Weimar, W. Göpel, A.c. measurements on tin oxide sensors to improve selectivities and sensitivities, Sensors Actuat. B Chem. 26 (1995) 13–18.
[64] S. Kumar, A. Kumar, P.K. Ahluwalia, A first principle study of bulk and electronic properties of "Ceria" using LDA + U method, AIP Conf. Proc. 1832 (2017) 90028, https://doi.org/10.1063/1.4980581.
[65] H. Ramanantoanina, A DFT-based theoretical model for the calculation of spectral profiles of lanthanide M4,5-edge x-ray absorption, J. Chem. Phys. 149 (2018) 54104, https://doi.org/10.1063/1.5043052.
[66] M. El Khalifi, F. Picaud, M. Bizi, Electronic and optical properties of CeO2 from first principles calculations, Anal. Methods 8 (2016) 5045–5052, https://doi.org/10.1039/C6AY00374E.
[67] D.R. Stull, H. Prophet, JANAF Thermochemical Tables. Washington, 1971.
[68] S. Chang, Oxygen chemisorption on tin oxide: Correlation between electrical conductivity and EPR measurements, J. Vac. Sci. Technol. 17 (1980) 366–369, https://doi.org/10.1116/1.570389.
[69] M.A. Ponce, R. Parra, R. Savu, et al., Impedance spectroscopy analysis of TiO2 thin film gas sensors obtained from water-based anatase colloids, Sensors Actuat., B Chem. 139 (2009) 447–452, https://doi.org/10.1016/j.snb.2009.03.066.
[70] M.A. Ponce, M.S. Castro, C.M. Aldao, Capacitance and resistance measurements of SnO2 thick-films, J. Mater. Sci. Mater. Electron. 20 (2008) 25–32, https://doi.org/10.1007/s10854-008-9590-8.
[71] C.H. Seager, G.E. Pike, Anomalous low-frequency grain-boundary capacitance in silicon, Appl. Phys. Lett. 37 (1980) 747–749, https://doi.org/10.1063/1.92019.
[72] G.E. Pike, Semiconductor grain-boundary admittance: theory, Phys. Rev. B 30 (1984) 795–802.
[73] A. Pfau, K.D. Schierbaum, The electronic structure of stoichiometric and reduced CeO2 surfaces: an XPS, UPS and HREELS study, Surf. Sci. 321 (1994) 71–80, https://doi.org/10.1016/0039-6028(94)90027-2.
[74] M. Matsumoto, K. Soda, K. Ichikawa, et al., Resonant photoemission study of CeO2, Phys. Rev. B 50 (1994) 11340–11346, https://doi.org/10.1103/PhysRevB.50.11340.
[75] J.W. Allen, Valence fluctuations in narrow band oxides, J. Magn. Magn. Mater. 47–48 (1985) 168–174, https://doi.org/10.1016/0304-8853(85)90388-9.
[76] G. Praline, B.E. Koel, R.L. Hance, et al., X-Ray photoelectron study of the reaction of oxygen with cerium, J. Electron. Spectros. Relat. Phenom. 21 (1980) 17–30, https://doi.org/10.1016/0368-2048(80)85034-1.
[77] A. Laachir, V. Perrichon, A. Badri, et al., Reduction of CeO2 by hydrogen. Magnetic susceptibility and Fourier-transform infrared, ultraviolet and X-ray photoelectron spectroscopy measurements, J. Chem. Soc. Faraday Trans. 87 (1991) 1601–1609, https://doi.org/10.1039/FT9918701601.
[78] B.M. Reddy, A. Khan, Y. Yamada, et al., Surface Characterization of CeO2/SiO2 and V2O5/CeO2/SiO2 catalysts by Raman, XPS, and other techniques, J. Phys. Chem. B 106 (2002) 10964–10972, https://doi.org/10.1021/jp021195v.
[79] D. Mullins, S. Overbury, D. Huntley, Electron spectroscopy of single crystal and polycrystalline cerium oxide surfaces, Surf. Sci. 409 (1998) 307–319, https://doi.org/10.1016/S0039-6028(98)00257-X.
[80] R. Eloirdi, P. Cakir, F. Huber, et al., X-ray photoelectron spectroscopy study of the reduction and oxidation of uranium and cerium single oxide compared to (U-Ce) mixed oxide films, Appl. Surf. Sci. 457 (2018) 566–571, https://doi.org/10.1016/j.apsusc.2018.06.148.
[81] M. Romeo, K. Bak, J. El Fallah, et al., XPS study of the reduction of cerium dioxide, Surf. Interface Anal. 20 (1993) 508–512, https://doi.org/10.1002/sia.740200604.
[82] E. Bêche, P. Charvin, D. Perarnau, et al., Ce 3d XPS investigation of cerium oxides

and mixed cerium oxide (CexTiyOz), in: Surface and Interface Analysis, 2008, pp. 264–267.
[83] B. Xu, Q. Zhang, S. Yuan, et al., Morphology control and characterization of broom-like porous CeO2, Chem. Eng. J. 260 (2015) 126–132, https://doi.org/10.1016/j.cej.2014.09.001.
[84] A. Kotani, T. Jo, J.C. Parlebas, Many-body effects in core-level spectroscopy of rare-earth compounds, Adv. Phys. 37 (1988) 37–85, https://doi.org/10.1080/00018738800101359.
[85] O. Gunnarsson, K. Schönhammer, Electron spectroscopies for Ce compounds in the impurity model, Phys. Rev. B 28 (1983) 4315–4341, https://doi.org/10.1103/PhysRevB.28.4315.
[86] N. Barsan, U. Weimar, Fundamentals of metal oxide gas sensors, in: MCS 2012 – 14th Int Meet Chem Sensors, 2012, pp. 618–621. https://doi.org/10.5162/IMCS2012/7.3.3.
[87] I. Kim, A. Rothschild, H.L. Tuller, Advances and new directions in gas-sensing devices.pdf. 61, 2013, pp. 974–1000.
[88] S.M.A. Durrani, M.F. Al-Kuhaili, I.A. Bakhtiari, Carbon monoxide gas-sensing properties of electron-beam deposited cerium oxide thin films, Sensors Actuat. B Chem. 134 (2008) 934–939, https://doi.org/10.1016/j.snb.2008.06.049.
[89] A. Sachdeva, S.V. Chavan, A. Goswami, et al., Positron annihilation spectroscopic studies on Nd-doped ceria, J. Solid State Chem. 178 (2005) 2062–2066, https://doi.org/10.1016/j.jssc.2005.04.016.
[90] H. Inaba, H. Tagawa, Ceria-based solid electrolytes, Solid State Ionics (1996) 1–16.
[91] K.C. Kao, Electrical conduction and photoconduction, in: Kao KCBT-DP in S (Ed.), Dielectric Phenomena in Solids. Academic Press, San Diego, 2004, pp. 381–514.
[92] H. Fröhlich, Electrons in lattice fields, Adv. Phys. 3 (1954) 325–361, https://doi.org/10.1080/00018735400101213.
[93] H. Fröhlich, H. Pelzer, S. Zienau, Properties of slow electrons in polar materials. London, Edinburgh, Dublin Philos. Mag. J. Sci. 41 (1950) 221–242, https://doi.org/10.1080/14786445008521794.
[94] K.C. Kao, Optical and electro-optic processes, in: Kao KCBT-DP in S (Ed.), Dielectric Phenomena in Solids. Academic Press, San Diego, 2004, pp. 115–212.